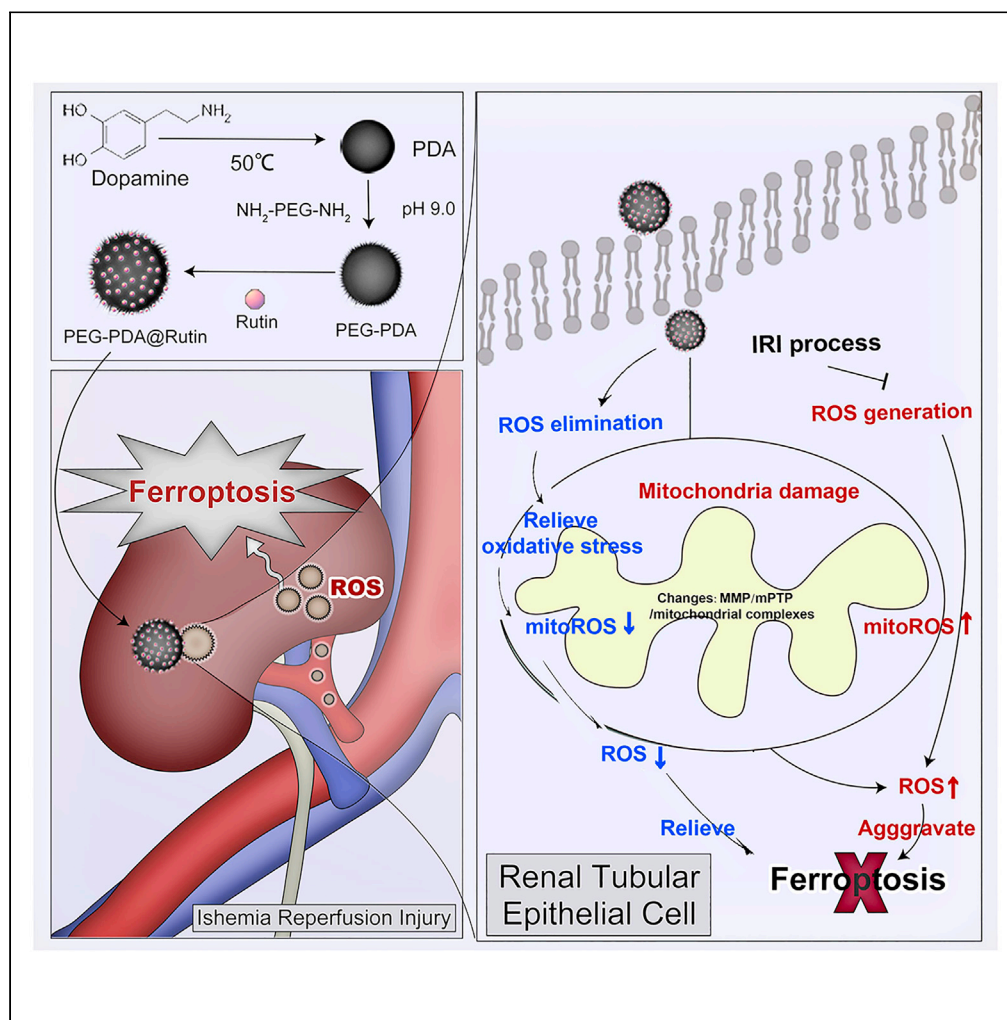Article

Melanin-like nanoparticles alleviate ischemia-reperfusion injury in the kidney by scavenging reactive oxygen species and inhibiting ferroptosis

Wenxiang Feng, Nan Zhu, Yubin Xia, ..., Song Zhou, Yongguang Liu, Ding Liu

23493313@qq.com (S.Z.)
liuyg168@smu.edu.cn (Y.L.)
banbybear01@smu.edu.cn (D.L.)

Highlights

PPR NPs were ~100 nm spherical particles with good ROS scavenging ability

PPR NPs could enter renal tubular cells and then release rutin to eliminate ROS

PPR NPs alleviate IRI damage by repairing mitochondria and suppressing ferroptosis

Article

Melanin-like nanoparticles alleviate ischemia-reperfusion injury in the kidney by scavenging reactive oxygen species and inhibiting ferroptosis

Wenxiang Feng,[1,4] Nan Zhu,[2,4] Yubin Xia,[3,4] Zehai Huang,[2,4] Jianmin Hu,[1] Zefeng Guo,[1] Yuzhuz Li,[1] Song Zhou,[1,*] Yongguang Liu,[1,*] and Ding Liu[1,5,*]

SUMMARY

Kidney transplantation is essential for patients with end-stage renal disease; however, ischemia-reperfusion injury (IRI) during transplantation can lead to acute kidney damage and compromise survival. Recent studies have reported that antiferroptotic agents may be a potential therapeutic strategy, by reducing production of reactive oxygen species (ROS). Therefore, we constructed rutin-loaded polydopamine nanoparticles (PEG-PDA@rutin NPs, referred to as PPR NPs) to eliminate ROS resulting from IRI. Physicochemical characterization showed that the PPR NPs were ~100 nm spherical particles with good ROS scavenging ability. Notably, PPR NPs could effectively enter lipopolysaccharide (LPS)-treated renal tubular cells, then polydopamine (PDA) released rutin to eliminate ROS, repair mitochondria, and suppress ferroptosis. Furthermore, *in vivo* imaging revealed that PPR NPs efficiently accumulated in the kidneys after IRI and effectively protected against IRI damage. In conclusion, PPR NPs demonstrated an excellent ability to eliminate ROS, suppress ferroptosis, and protect kidneys from IRI.

INTRODUCTION

Kidney transplantation is the most effective therapy option for the majority of patients with end-stage renal disease (ESRD). However, the inevitable ischemia-reperfusion injury (IRI) in the donor kidney during transplantation sets serious obstacles to a favorable prognosis and contributes to various pathological processes. Previous studies indicated that IRI could cause damage to renal tubular epithelial cell (TEC), resulting in acute kidney injury, delayed graft function, and rejection reactions, all of which are crucial factors affecting the early functional recovery and long-term survival of the transplanted kidney.[1] In particular, excessive reactive oxygen species (ROS) is generated after IRI, leading to severe injuries inside renal TEC.[2] According to the latest research, ROS, as a cytotoxic substance, can oxidize unsaturated fatty acids into lipid peroxides by iron catalysis, thereby disrupting the cell membrane structure of TEC.[3–6] This suggests that eliminating ROS and inhibiting ferroptosis may be potent strategies for preventing and treating kidney IRI.

The development of safer and more efficient ROS-scavenging pharmaceuticals is a primary research objective. Rutin, a flavonoid glycoside component isolated from Sophora japonica (Japanese pagoda trees), is widely employed to treat hypertension, diabetes, and cardiovascular diseases, owing to its powerful antioxidant activity and minimal side effects.[7,8] According to previous research,[9] rutin could effectively ameliorate inflammation and fibrosis in unilateral uretera obstruction (UUO) rats, reduce renal oxidative stress damage by inhibiting the activation of NF-κB and TGF-β1/Smad3 signaling pathways, and alleviate IRI-related kidney injury. Nevertheless, the clinical implementation of rutin is hindered by several shortcomings, including easy decomposition, allergenicity, and poor bioavailability. Exploiting a system that can deliver rutin to transplant kidney was therefore the key to improve the therapeutic efficacy of rutin.

Polydopamine (PDA), which is derived from marine mussels, has excellent potential in drug delivery due to its good biodegradability, simple preparation, and drug-loading methods.[10–13] In the meantime, the PDA's catechol structure enables it to purge ROS.[14,15] This suggests that the combination of rutin and melanin-like nanoparticles (NPs)[16] could be a promising strategy for protection against ROS[17] and ferroptosis in IRI, despite the fact that this combination has not yet been established.

In this study, we constructed rutin-loaded polydopamine nanoparticles (PEG-PDA@rutin NPs, referred to as PPR NPs) and analyzed their particle size distribution, zeta potential, drug release curves, and ROS scavenging characteristics using Fourier transform infrared (FT-IR)

[1]Department of Organ Transplantation, Zhujiang Hospital, The Second School of Clinical Medicine, Southern Medical University, Guangzhou, Guangdong 510515, China
[2]Nanfang Hospital, The First School of Clinical Medicine, Southern Medical University, Guangzhou, Guangdong 510515, China
[3]Department of Nephrology, First Affiliated Hospital of Shantou University Medical College, No. 57, Changping Rd, Shantou, Guangdong Province 515000, China
[4]These authors contributed equally
[5]Lead contact
*Correspondence: 23493313@qq.com (S.Z.), liuyg168@smu.edu.cn (Y.L.), banbybear01@smu.edu.cn (D.L.)
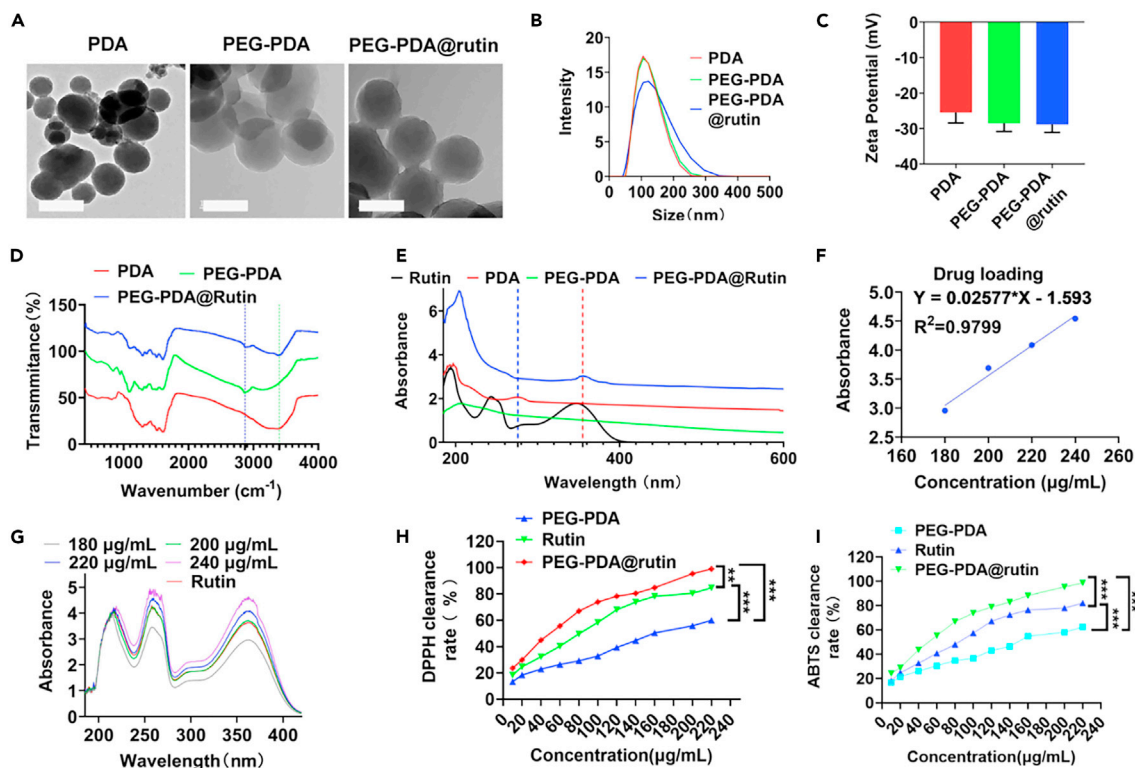https://doi.org/10.1016/j.isci.2024.109504

Figure 1. Characterization of PPR NPs

(A) TEM images of PDA, PP, and PPR NPs.

(B) DLS distribution of PDA, PP, and PPR NPs.

(C) Zeta potentials of PDA, PP, and PPR NPs.

(D) FI-IR analysis of PDA, PP, and PPR NPs.

(E) UV-Vis analysis of PDA, PP, and PPR NPs.

(F) The dose curve of rutin, detected by UV-Vis spectrophotometer at 350 nm.

(G) UV-Vis analysis of rutin.

(H) DPPH clearance of rutin, PP, and PPR NPs.

(I) ABTS clearance of rutin, PP, and PPR NPs. n = 3. ***$p < 0.001$. Data are represented as mean ± SEM.

spectroscopy and ultraviolet-visible (UV-Vis) spectroscopy. During *in vitro* and *in vivo* experiments, we observed that PPR NPs could enter LPS-treated renal tubular cells and IRI kidneys of mice, eliminate ROS, repair mitochondria, suppress ferroptosis, reduce cell death, and protect kidneys from IRI damage. Overall, our study suggests that PPR NPs could serve as a therapeutic choice for the clinical treatment of IRI during kidney transplantation.

RESULTS

Preparation and characterization of PPR NPs

Scheme 1 shows the design and synthesis of the PDA NPs functionalized with PEG as a ligand and loaded with rutin. PDA was chosen as the carrier owing to its easy functionalization and low cytotoxicity;[18] it could increase the water insolubility of rutin and thereby enhance the ability to clear ROS. Firstly, the PDA NPs were synthesized via oxidative polymerization in an alkaline environment. To improve stability, the PDA NPs were modified with PEG. To measure the particle stability, same concentrations of PDA, PP, and PPR NPs at 0, 1, 3, and 7 days were summarized in *Supplementary file*, Figure S1. PP NPs and PPR NPs remained stable in PBS after 7 days, whereas PDA NPs had precipitated. These results confirmed the improved stability of PDA NPs upon PEG modification. To verify the successful synthesis of PPR NPs, we used TEM, DLS, zeta potential, UV-Vis, and FT-IR analyses. The TEM and DLS results showed that PDA, PEG-PDA (referred to as PP), and PPR NPs exhibited a ~120 nm uniform and well-dispersed spherical shape (Figures 1A and 1B, *Supplementary file;* Figure S2). PDA NPs showed negative zeta potential (−25.3 mV), consistent with the conclusion that dopamine polymerization dissociates quinone and imine groups under alkaline conditions, resulting in a negatively charged surface. The zeta potential of the PP NPs (−29.6 mV) indicated that PEG modification improved suspension stability. As rutin itself does not carry a charge, there was no significant difference in zeta potential between PPR NPs (−30 mV) and PP NPs (Figure 1C). The FT-IR results showed that compared to PDA, a new peak at 2,890 cm^{-1} was observed in PP group, indicating that PEG is
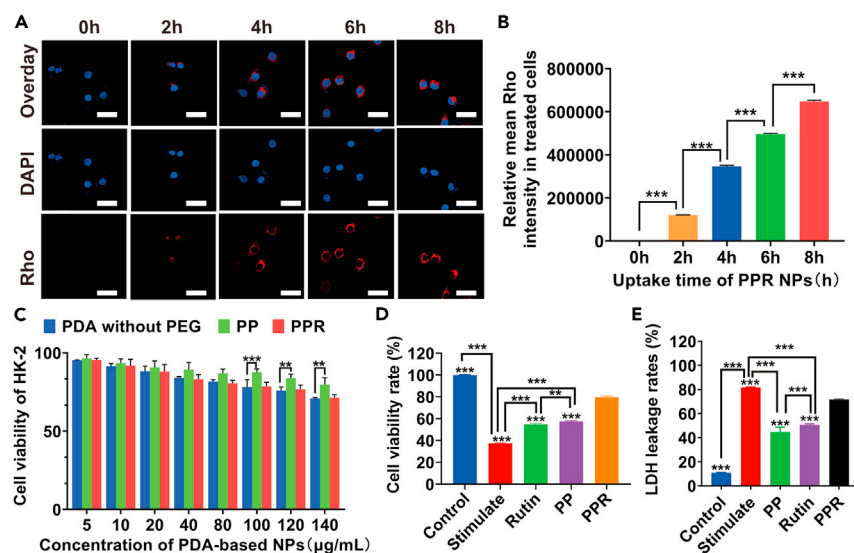
Figure 2. *In vitro* cellular uptake and biocompatibility of PPR NPs
(A and B) CLSM images of HK-2 cells, after being incubated with Rho labeled PRP NPs for 1–8 h (left) and their statistic intensities (right). Scar bar, 30 μm.
(C) Cell viabilities of HK-2 cells, after being incubated with PDA, PP, and PPR NPs, using CCK-8 assay.
(D) Cell viabilities of LPS-induced HK-2 cells, after being incubated with PP and PPR NPs, using CCK-8 assay.
(E) LDH leakage of LPS-induced HK-2 cells, after being incubated with PP and PPR NPs, using Elisa assay. n = 3. **p < 0.01, ***p < 0.001. Data are represented as mean ± SEM.

bound to PDA.[19] Furthermore, a new peak at approximately 3,400 cm^{-1}, belonging to the hydroxyl stretching vibration of rutin,[20] was observed in the PRP group (Figure 1D), indicating that rutin was successfully loaded onto the PP NPs. Similarly, the UV-Vis spectra showed a characteristic absorption peak at 359 nm for PPR NPs, indicating the successful binding of rutin to PP NPs (Figure 1E). To calculate the loading efficiency (LE%) of rutin in PPR NPs, we constructed a standard curve relating concentration of rutin. By detecting the absorbance of the drug-loaded supernatant, we determined that the supernatant contained 13 mg of rutin, with the remaining 12 mg of rutin bound to 25 mg of PP, resulting in a calculated LE% of 48% (Figures 1F and 1G). These results indicated that the modification of PEG could improve the dispersion stability of PPR NPs compared to that of pure PDA NPs, and rutin was successfully bound to the PP NPs. To measure the degrading characteristics of PPR NPs under ROS stimulation, same concentrations of PPR NPs were placed in PBS and 500 μM H_2O_2 at room temperature for 0, 2, 4, 6, 8, and 10 h. As summarized in *Supplementary file*, Figure S3, PPR NPs remained stable in PBS, whereas PPR NPs had significantly disintegrated in 500 μM H_2O_2. Since that, we further detected the drug releasing capacity of rutin in PPR NPs in PBS or ROS condition. As shown in *Supplementary file*, Figures S4–S6, only about 30% of rutin was released within 8 h at PBS solution. In contrast, the release of rutin reached nearly 93% within 8 h at H_2O_2 solution, which demonstrates that the release of rutin could be accelerated in ROS condition. These results confirmed PPR NPs could resolve at ROS-enriching environment and indicating that rutin could be released rapidly in IRI environments with oxidative stress to achieve better therapeutic effect.

To verify the antioxidant activity of PPR NPs, different concentrations of rutin, PP, and PPR were added to DPPH and ABTS configurations. After the reaction was completed, the supernatant was added to a 96-well plate, and absorbance was measured using an enzyme marker.[21] Both DPPH and ABTS experiments showed that PP, rutin, and PPR exhibited ROS clearance in a dose-dependent manner (Figures 1H and 1I). To date, the scavenging rate of PPR was lower than the sum of rutin and PP, which might contribute from the bound status of rutin and PP. Under the incubation condition (30 min), the loading rutin was still not fully released, making to its compromised antioxidant effect. To address these issues, we further increased concentration of rutin, PP, and PPR, and we found that compared to free rutin and PP, only PPR did achieve a 100% clearance rate (Figures 1H and 1I). Furthermore, since 90% of rutin release from PPR could be achieved at 500 μmoL H_2O_2 solution within 12 h, we subsequently pre-incubated PPR at 500 μmoL H_2O_2 condition for 12 h, then added them into DPPH and ABTS solutions. From *Supplementary file*, Figures S7 and S8, we found that PPR achieved ∼85% clearance rate, which was higher than the efficiency of rutin (∼35%) plus PP (∼26%) under the same concentration condition. Therefore, we believed that though the total ROS clearance rate of PPR was relatively lower at a shorter time, but PPR could exert a more effective effect in the body with longer time.

In vitro cellular uptake and biocompatibility of PPR NPs

In recent years, extensive researches have shown that nanotechnology could achieve effective intracellular drug delivery.[22] Melanin and its analogs have strong biocompatibility and are therefore widely used as drug-release platforms.[23,24] Moreover, the surface contains multiple modifiable functional groups, enabling efficient binding to different drugs for the efficient delivery of medications. To determine the uptake ability of the PPR NPs, they were labeled with red fluorescent dye based on a molar ratio of 2:1. As shown in Figures 2A and 2B, LPS-treated

HK-2 cells were exposed to PPR NPs for 0–8 h and subsequently stained with DAPI to visualize nuclei. Confocal laser scanning microscope (CLSM) images and a quantitative analysis revealed that LPS-treated HK-2 cells absorbed substantial amounts of the drug at 8 h, as the PPR NPs occupied most of the cytoplasmic space. Therefore, based on the CLSM results, the PPR NPs could be easily absorbed by HK-2 cells, resulting in a high rutin uptake efficiency. To evaluate the biocompatibility of PPR NPs produced in this study, the viability of HK-2 cells was assessed after incubation with PPR NPs. CCK-8 assay demonstrated that HK-2 cells treated with PP and PPR NPs had survival rates of >75% (Figure 2C), indicating good biocompatibility. Compared with the viability of cells treated with PP NPs, free PDA inhibited lower level of cell viability, as PEG modification increased stability and safety. These findings suggest that PPR NPs are good drug release systems with biomedical applications.

To investigate the protective effect of PPR, 100 μL of rutin, PP, and PPR NPs were added to LPS-treated HK-2 cells. The CCK-8 and LDH results revealed a significant decrease in cell viability and a sharp increase in LDH leakage in LPS group compared to those in control group (Figures 2D and 2E). However, cell viability and LDH leakage were significantly rescued in the presence of PP and PPR NPs, with PPR showing the most significant improvement, indicating the protective effect of PPR NPs on LPS-treated HK-2 cells. Additionally, we used a hypoxic culture box to simulate a hypoxia model, and the CCK-8 result consistently indicated that PPR NPs had a protective effect on renal tubular epithelium (*Supplementary file*, Figure S9). To date, CCK-8 and LDH results also showed that rutin did have a certain protective effect, but its effect was relatively poor, compared to PPR. Our results suggested that PP, as a nano-carrier, could greatly increase the bioavailability of rutin.

Intracellular antioxidant activity of PPR NPs

When tissues undergo IRI, cellular metabolic homeostasis is disrupted. The tricarboxylic acid cycle is interrupted under a lack of oxygen, metabolic products in the TCA cycle accumulate, and succinic acid, a metabolic intermediate in the TCA cycle,[25] accumulates selectively during ischemia. Subsequently, large amounts of ROS are generated during reperfusion. ROS oxidizes phosphatidylserine on the cell membrane under the action of an unstable iron pool within the cell, ultimately causing cell membrane damage and ferroptosis.[26] Therefore, removing ROS from the source can effectively reduce ferroptosis.

Extensive researches have shown that rutin not only scavenges ROS directly owing to its chemical structure, but also increases the production of GSH and antioxidant enzymes, such as catalase (CAT) and superoxide dismutase (SOD),[27] and inhibits xanthine oxidase (involved in ROS production). Therefore, rutin has extensive pharmacological applications, with antioxidant, anti-inflammatory, cardiovascular, neuroprotective, antidiabetic, and anticancer activities.[28] Furthermore, because they scavenge various reactive oxygen and nitrogen species, artificial PDA nanoparticles have been widely applied in the antioxidant treatment of many ROS-related diseases. Recently, Liu et al. found that melanin nanoparticles alleviated sepsis-induced myocardial injury by suppressing ferroptosis and inflammation caused by melanin-like nanoparticles.[29] Consequently, PPR may exert strong anti-ROS effects. To verify this prediction, HK-2 cells were divided into four groups, including a control, stimulated (LPS), PP, and PPR group, and DCFH-DA was used to label ROS. CLSM images (Figure 3A) and a quantitative analysis of fluorescence intensity (Figure 3B) showed that ROS levels in the LPS-induced group were significantly higher than those in the control group. Due to the ROS removal ability of PDA, the ROS levels in the PP group were significantly lower than those in the positive control, and the ROS levels in the PPR group were lower than those in the PP group. These results demonstrate that PPR NPs have good intracellular ROS removal ability. To verify whether our PPR NPs could protect cells by reducing lipid peroxidation levels, cells were stained with BODIPY 581/591 C11 probes; the probe color changes from red to green under conditions of increased lipid peroxidation. As shown in Figures 3C–3E, lipid peroxidation levels were significantly higher in the stimulated group than in the control group. The amounts of reduced glutathione were lower in the PP and PRP groups than in the stimulated group but were significantly higher than those in the positive group. In the PPR NP group, the amount of lipid peroxidation was suppressed to a greater extent than in the PP intervention group. These results indicate that PPR NPs can stably exert their antioxidant effects in cells and effectively reduce lipid peroxidation, thereby reducing cell death under pathological conditions of ischemia-reperfusion.[30]

Effects of PPR NPs on mitochondrial repair

When the kidney undergoes IRI during transplantation, cardiolipin on the mitochondrial membrane is oxidatively damaged, resulting in the dissociation of complexes I and III from the supercomplex, which causes ETC electron leakage and the breakdown of the steady-state mitoROS.[31] The decrease in mitochondrial membrane potential (MMP) due to IRI leads to damage to the mitochondrial complex, opening the mPTP(mitochondrial permeability transition pore) channel, and triggering RIRR (a series of pathological injuries caused by increased ROS leading to massive ROS release).[32,33] This results in the disruption of normal mitochondrial metabolism and the accumulation and generation of mitoROS, the main source of intracellular ROS. Ultimately, ROS are released into the cytoplasm and, in the presence of catalytic iron ions in the variable iron pool within the cell, oxidize polyunsaturated phospholipids on the cell membrane, resulting in cell membrane damage and rupture.

We further evaluated whether PPR NPs can inhibit pathological injuries and protect renal tubular epithelial cells from ferroptosis after IRI. As shown in Figures 4C and 4D, mitoROS in the stimulated group showed a dramatic increase in fluorescence intensity compared to that in the control group, while a significant decrease was observed in the PP (~45%) and PPR (~55%) groups compared to LPS-treated HK-2 cells. Thus, it can be inferred that PPR NPs could efficiently penetrate the mitochondrial membrane and remove mitoROS. To verify whether PPR NPs could maintain the function of mitochondrial complexes by eliminating oxidative damage during IRI, cells were treated with the corresponding mitochondrial complex activity detection dyes. As determined by ELISA (Figures 4E–4H), both PP NPs and PPR NPs effectively reduced the
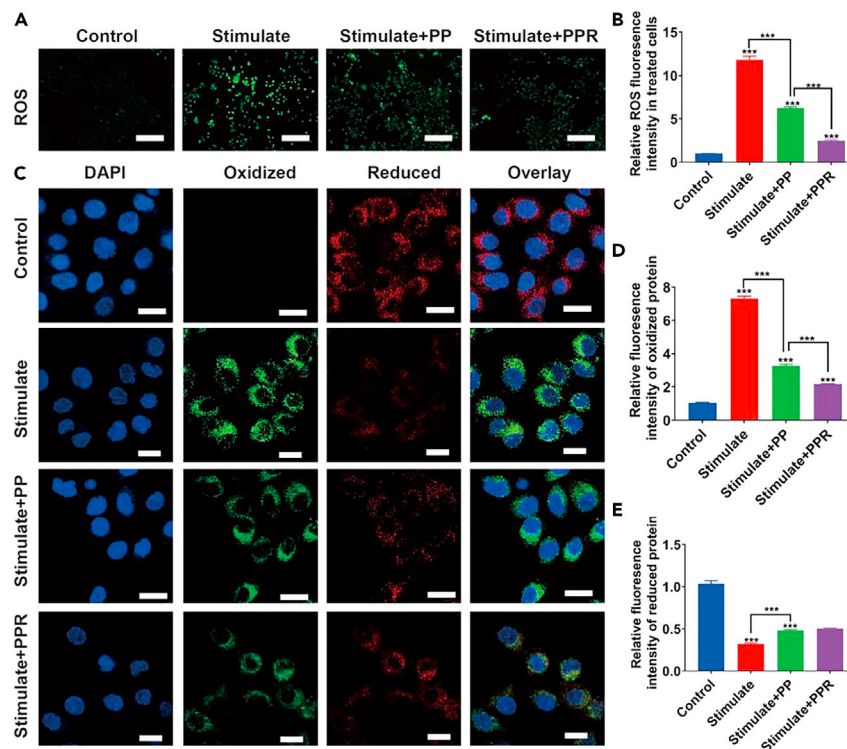
Figure 3. Intracellular antioxidant activity of PPR NPs

(A and B) CLSM images of ROS inside LPS-stimulated HK-2 cells, after being incubated with PP and PPR NPs (left) and their statistic intensities (right). Scar bar, 200 μm.

(C–E) CLSM images of oxidized and reduced proteins inside LPS-stimulated HK-2 cells, after being incubated with with PP and PPR NPs (left), and their statistic intensities (right). Scar bar, 100 μm. n = 3. ***p < 0.001. Data are represented as mean ± SEM.

damage to mitochondrial complexes (I, III, IV, and V) caused by LPS, suggesting that they can reduce the oxidative damage caused by mitochondrial complex dysfunction and decrease the excessive production of ROS to protect cells from ferroptosis.

MMP is an effective biomarker for evaluating mitochondrial function, and a decrease indicates changes in mitochondrial membrane permeability.[31] To further verify the inhibitory effect of PPR NPs on ROS-induced mitochondrial oxidative stress, we conducted a cell fluorescence experiment to evaluate the stabilizing effect on MMPs by the JC-1 probe, where a decrease in mPTP is indicated by a decrease in red fluorescence or an increase in the green/red ratio. As shown in Figure 4A, compared to levels of fluorescence in the control group, the positive control group showed a significant decrease in red fluorescence and a significant increase in green fluorescence. In the PP NP group, we observed a slight decrease in green fluorescence and a significant increase in red fluorescence compared to those in the positive control group, and these changes were rescued by PP NPs. This phenomenon was more pronounced in the PPR NP group. Therefore, PPR NPs regulate mPTP to reduce mitochondrial damage, thereby regulating oxidative metabolism and reducing ROS production in renal tubular epithelial cells to reduce ferroptosis.

Mitochondrial permeability transition pore (mPTP), widely distributed on the mitochondrial membrane, is a key channel in RIRR.[34] When ROS inside the mitochondria reach a threshold level, they trigger mPTP opening, leading to the collapse of the mPTP and a rapid increase in ROS production. In our study, Calcein AM was used to stain the mPTP, and the green fluorescence level of the positive control group induced by LPS was significantly decreased (Figure 4B). In the intervention group, the fluorescence intensities of both the PP and PPR groups were higher than that in the stimulated group, and the intensity of the PPR group was stronger than that of the PP group, indicating that PPR successfully inhibited mPTP opening, thereby reducing ROS release via the RIRR pathway.

In vivo enrichment and IRI alleviate the effect of PPR NPs

In this study, IR820 was encapsulated in PPR NPs. IRI mice were first established and subsequently treated with PPR NPs via tail vein injection to study the *in vivo* biodistribution. Using a small-animal *in vivo* fluorescence imaging system, we found that compared with the control kidney, a dramatic fluorescence signal of IR820 accumulated on the IRI kidney side. At 8 h after injection, we euthanized the mice using pentobarbital and collected various organs (heart, liver, spleen, lungs, kidneys, and brain) for fluorescence imaging. The results were consistent with those of the *in vivo* experiments, as the PPR NPs were mainly aggregated in the liver and kidneys. Moreover, the fluorescence signal in the kidneys of
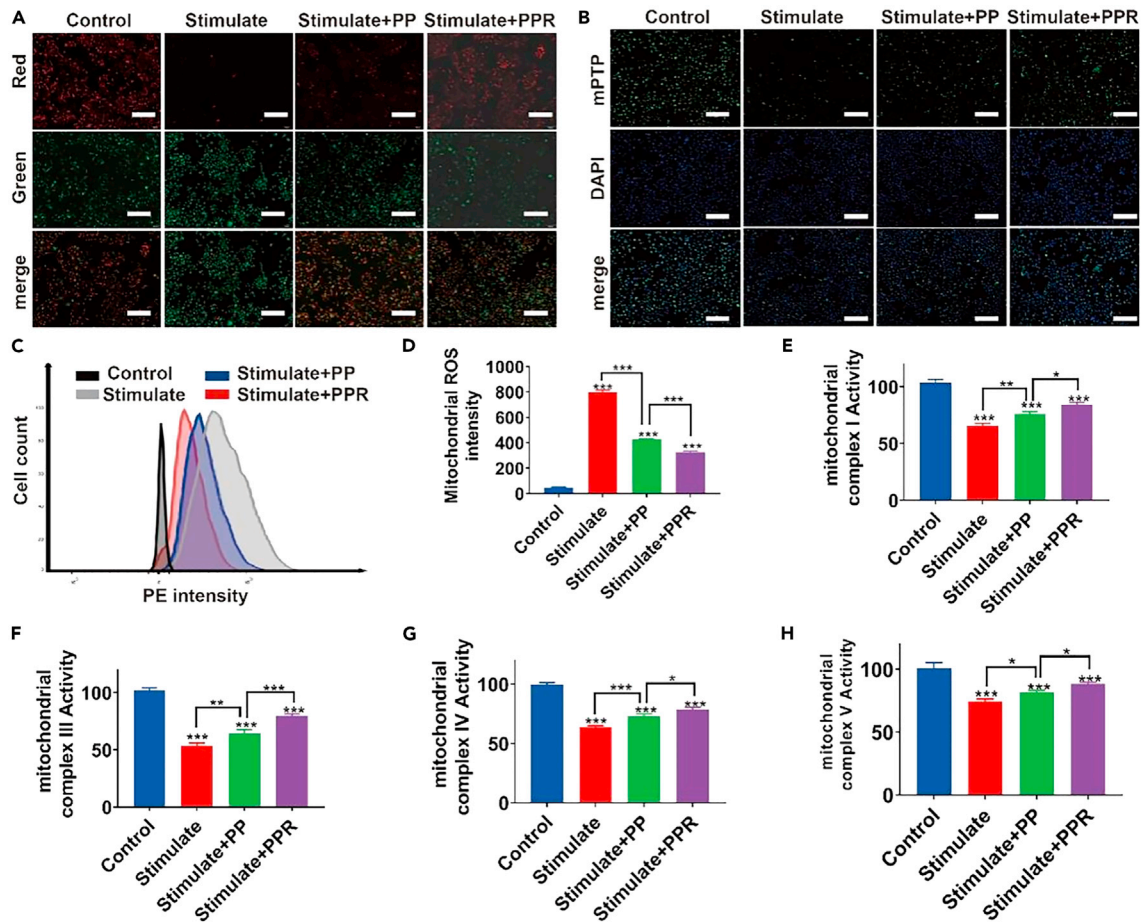
Figure 4. Effects of PPR NPs on mitochondrial repair

(A) CLSM images of JC-1 inside LPS-stimulated HK-2 cells, after being incubated with PP and PPR NPs (left), and their statistic intensities (right). Scar bar, 200 μm.

(B) CLSM images of mPTP inside LPS-stimulated HK-2 cells, after being incubated with PP and PPR NPs (left), and their statistic intensities (right). Scar bar, 200 μm.

(C and D) Flow cytometry images of mitoROS inside LPS-stimulated HK-2 cells, after being incubated with = PP and PPR NPs (left), and their statistic intensities (right).

(E–H) The expression mitochondrial complex I, III, IV, and V inside LPS-stimulated HK-2 cells, after being incubated with with PP and PPR NPs. n= 3. *p < 0.05. **p < 0.01. ***p < 0.001. Data are represented as mean ± SEM.

the IRI model was significantly stronger than that of the control kidney (Figures 5A and 5B). This indicates that the PRP NP nanodrug system aggregates in damaged kidneys, which helps protect the kidneys.

In clinical practice, renal IRI is one of the most common causes of acute kidney injury. Due to the strong compensatory function of the kidneys, mild and transient acute renal ischemia often leads to a reversible decline in renal function. However, prolonged ischemia and oxygen deprivation in the kidneys, which cannot be promptly corrected or repaired, can result in progressive renal fibrosis and CKD. Since PPR NPs were efficiently enriched in IRI kidneys, we further analyzed the protective effects of PPR NPs in vivo. Mice were divided into four groups: control, stimulated (IRI model), stimulated + PP (IRI model treated with PP NPs), and stimulated + PPR (IRI model treated with PPR NPs). After the treatment, we collected blood samples from all treated mice for kidney function tests. As shown in Figure 5C, CRE levels were extremely higher in the stimulated group than in the control group, while PP (∼60%) and PPR (∼75%) significantly downregulated CRE, demonstrating that the PRP nanodrug system could alleviate the degree of renal function damage in model mice to some extent.

Renal fibrosis is a major cause of CKD following renal IRI. To verify whether PRP could reduce renal interstitial fibrosis, kidney sections were subjected to HE and Masson's trichrome staining. Compared to the phenotype in the sham group, the renal tubular epithelial cells in the IRI group were swollen and necrotic, with obvious tubular formation and fibrosis (Figures 5D, 5F, and 5G). Compared with observations in the stimulated group, renal morphological damage and the degree of fibrosis were significantly reduced in the PP and PPR groups, and PPR NPs protected the kidneys and reduced damage to a greater extent. To verify whether our PPR NPs protected the IRI kidney from ferroptosis, the organs were subjected to immunohistochemistry (IHC) (GPX4) staining (Figures 5E and 5H). The expression of GPX4 in renal tubular cells treated with PPR NPs was significantly higher than that in stimulated group, indicating that the PPR NPs exerted an antioxidant effect and
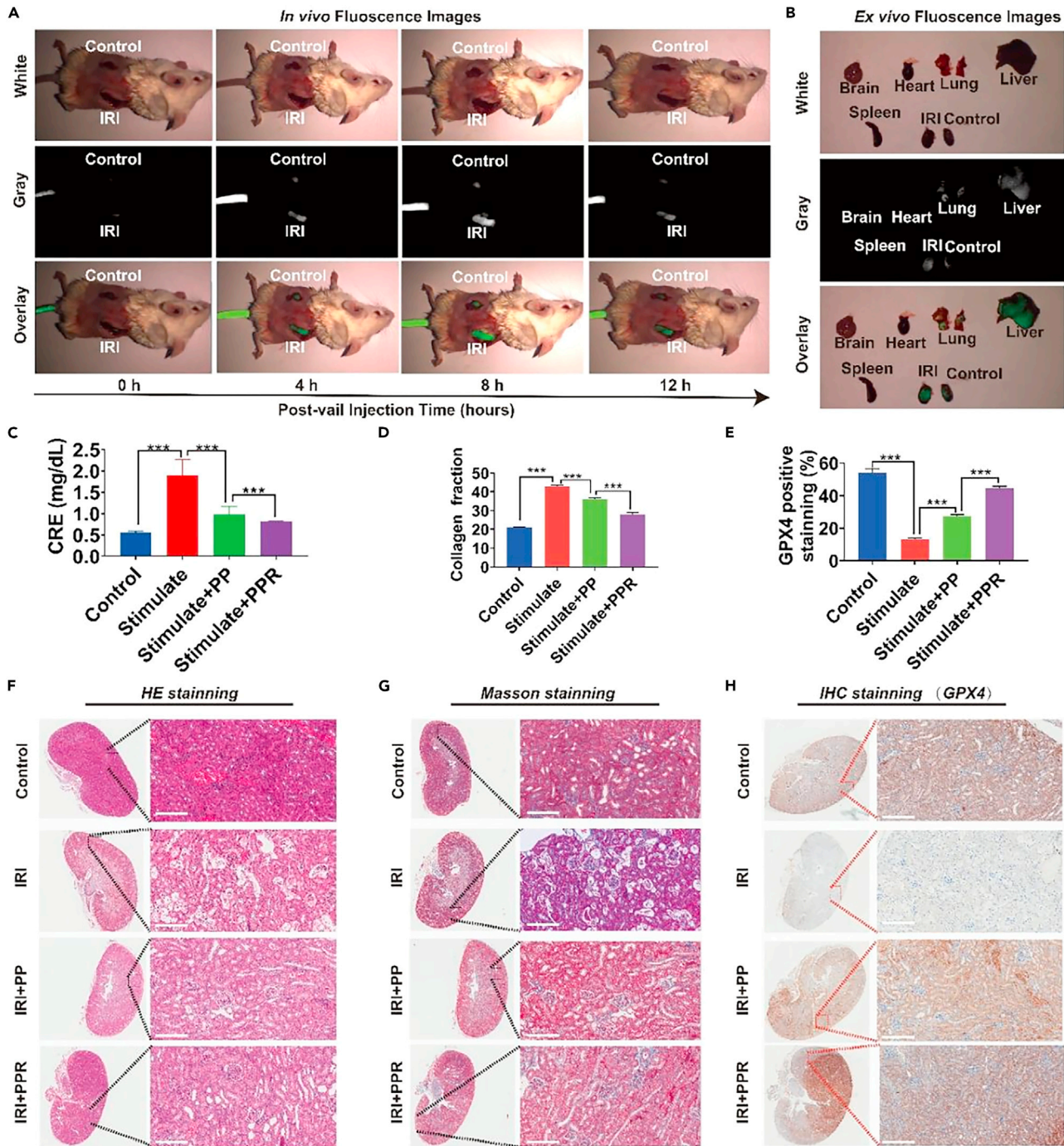
Figure 5. *In vivo* enrichment and IRI alleviate the effect of PPR NPs
(A) *In vivo* distribution of PPR NPs inside IRI mice.
(B) *Ex vivo* distribution of PPR NPs inside the major organs of IRI mice.
(C) The content of CRE in IRI mice's blood.
(D) The expression of collagen fraction of IRI mice, according to (G).
(E) The expression of GPX4 of IRI mice, according to (H).
(F–H) HE, Masson, and IHC staining of IRI mice's kidneys. n = 3. ***p < 0.001. Data are represented as mean $\pm$ SEM.

protected the tubular cells from ferroptosis, effectively preserving the function of the transplanted kidney. Taken together, these *in vivo* results confirmed that PPR NPs could efficiently enter the IRI kidney, effectively mitigating oxidative stress and protecting the kidney from IRI damage.

DISCUSSION

In summary, we developed a nanomedicine delivery system (refer to PPR NPs) consisting of PDA, PEG, and loaded rutin. PPR NPs were ~100 nm spherical particles with ROS-accelerated drug release and good ROS scavenging capacities. *In vitro* experiments supported its protective effects on renal tubules in IRI kidneys, by inhibiting excessive ROS production, repaired mitochondria, suppressed ferroptosis, and rescued cell viability. Furthermore, *in vivo* studies revealed that PPR NPs could efficiently accumulate in the kidneys after IRI and effectively protect against IRI damage to some extent. In conclusion, PPR NPs demonstrated a promising strategy of combat ROS during IRI and protect kidneys undergoing planation.

Limitations of the study

Though the therapeutic effect of PPR NPs was verified *in vitro* and *in vivo* experiments, their pharmacokinetics is still unclear. Furthermore, PPR could only passively accumulate into the kidney during blood circulation, lacking kidney targeting ability. In our next job, we would try to increase the organ-targeting capacity of PPR and investigate the metabolic processes.

STAR★METHODS

Detailed methods are provided in the online version of this paper and include the following:

- KEY RESOURCES TABLE
- RESOURCE AVAILABILITY
  - Lead contact
  - Materials availability
  - Data and code availability
- EXPERIMENTAL MODEL AND STUDY PARTICIPANT DETAILS
  - Mouse treatment
  - Animal model construction
  - Mice and ethics approval
  - Cell lines and primary cell cultures
- METHOD DETAILS
  - Synthesis of PDA
  - Surface modification of PDA with NH2-PEG-NH2
  - Rutin loading
  - Drug loading of PEG-PDA@rutin
  - Drug release assay of PEG-PDA@rutin
  - Characterization of PDA-based nanoparticles
  - Cell culture
  - Cellular uptake
  - Cell toxicity
  - ROS removal experiment
  - Ferroptosis detection
  - Mitochondrial status detection
  - *In vivo* distribution of PPR NPs on IRI mice
  - Mouse sample collection and renal function testing
  - Histological examination and renal tubular injury scoring
- QUANTIFICATION AND STATISTICAL ANALYSIS

SUPPLEMENTAL INFORMATION

Supplemental information can be found online at https://doi.org/10.1016/j.isci.2024.109504.

ACKNOWLEDGMENTS

REFERENCES

1. Liao, X., Lv, X., Zhang, Y., Han, Y., Li, J., Zeng, J., Tang, D., Meng, J., Yuan, X., Peng, Z., et al. (2022). Fluorofenidone Inhibits UUO/IRI-Induced Renal Fibrosis by Reducing Mitochondrial Damage. Oxid. Med. Cell. Longev. *2022*, 2453617. https://doi.org/10.1155/2022/2453617.

2. Minami, K., Bae, S., Uehara, H., Zhao, C., Lee, D., Iske, J., Fanger, M.W., Reder, J., Morrison, I., Azuma, H., et al. (2020). Targeting of intragraft reactive oxygen species by APP-103, a novel polymer product, mitigates ischemia/reperfusion injury and promotes the survival of renal transplants. Am. J. Transplant *20*, 1527–1537. https://doi.org/10.1111/ajt.15794.

3. Niu, B., Liao, K., Zhou, Y., Wen, T., Quan, G., Pan, X., and Wu, C. (2021). Application of glutathione depletion in cancer therapy: Enhanced ROS-based therapy, ferroptosis, and chemotherapy. Biomaterials *277*, 121110. https://doi.org/10.1016/j.biomaterials.2021.121110.

4. Stockwell, B.R. (2022). Ferroptosis turns 10: Emerging mechanisms, physiological functions, and therapeutic applications. Cell *185*, 2401–2421. https://doi.org/10.1016/j.cell.2022.06.003.

5. Wei, R., Zhao, Y., Wang, J., Yang, X., Li, S., Wang, Y., Yang, X., Fei, J., Hao, X., Zhao, Y., et al. (2021). Tagitinin C induces ferroptosis through PERK-Nrf2-HO-1 signaling pathway in colorectal cancer cells. Int. J. Biol. Sci. *17*, 2703–2717. https://doi.org/10.7150/ijbs.59404.

6. Wu, C., Liu, Z., Chen, Z., Xu, D., Chen, L., Lin, H., and Shi, J. (2021). A nonferrous ferroptosis-like strategy for antioxidant inhibition-synergized nanocatalytic tumor therapeutics. Sci. Adv. *7*, eabj8833. https://doi.org/10.1126/sciadv.abj8833.

7. Muvhulawa, N., Dludla, P.V., Ziqubu, K., Mthembu, S.X.H., Mthiyane, F., Nkambule, B.B., and Mazibuko-Mbeje, S.E. (2022). Rutin ameliorates inflammation and improves metabolic function: A comprehensive analysis of scientific literature. Pharmacol. Res. *178*, 106163. https://doi.org/10.1016/j.phrs.2022.106163.

8. Ouyang, Q., Liu, K., Zhu, Q., Deng, H., Le, Y., Ouyang, W., Yan, X., Zhou, W., and Tong, J. (2022). Brain-Penetration and Neuron-Targeting DNA Nanoflowers Co-Delivering miR-124 and Rutin for Synergistic Therapy of Alzheimer's Disease. Small *18*, e2107534. https://doi.org/10.1002/smll.202107534.

9. Wang, B., Liu, D., Zhu, Q.-H., Li, M., Chen, H., Guo, Y., Fan, L.-P., Yue, L.-S., Li, L.-Y., and Zhao, M. (2016). Rutin ameliorates kidney interstitial fibrosis in rats with obstructive nephropathy. Int. Immunopharmacol. *35*, 77–84. https://doi.org/10.1016/j.intimp.2016.03.029.

10. Li, H., Yin, D., Li, W., Tang, Q., Zou, L., and Peng, Q. (2021). Polydopamine-based nanomaterials and their potentials in advanced drug delivery and therapy. Colloids Surf. B Biointerfaces *199*, 111502. https://doi.org/10.1016/j.colsurfb.2020.111502.

11. Niezni, D., Harris, Y., Sason, H., Avrashami, M., and Shamay, Y. (2022). Polydopamine Copolymers for Stable Drug Nanoprecipitation. Int. J. Mol. Sci. *23*, 12420. https://doi.org/10.3390/ijms232012420.

12. Lu, J., Gao, X., Wang, S., He, Y., Ma, X., Zhang, T., and Liu, X. (2023). Advanced strategies to evade the mononuclear phagocyte system clearance of nanomaterials. Exploration *3*, 20220045. https://doi.org/10.1002/EXP.20220045.

13. Xiang, H., Yan, H., Liu, J., Cheng, R., Xu, C.-Q., Li, J., and Yao, C. (2022). Identifying the Real Chemistry of the Synthesis and Reversible Transformation of AuCd Bimetallic Clusters. J. Am. Chem. Soc. *144*, 14248–14257. https://doi.org/10.1021/jacs.2c05053.

14. Zhang, Y., Ren, X., Wang, Y., Chen, D., Jiang, L., Li, X., Li, T., Huo, M., and Li, Q. (2021). Targeting Ferroptosis by Polydopamine Nanoparticles Protects Heart against Ischemia/Reperfusion Injury. ACS Appl. Mater. Interfaces *13*, 53671–53682. https://doi.org/10.1021/acsami.1c18061.

15. Mavridi-Printezi, A., Menichetti, A., Mordini, D., Amorati, R., and Montalti, M. (2023). Recent Applications of Melanin-like Nanoparticles as Antioxidant Agents. Antioxidants *12*, 863. https://doi.org/10.3390/antiox12040863.

16. Zhao, Y., Zhang, Z., Pan, Z., and Liu, Y. (2021). Advanced bioactive nanomaterials for biomedical applications. Exploration *1*, 20210089. https://doi.org/10.1002/EXP.20210089.

17. Huang, C., Wang, X., Yang, P., Shi, S., Duan, G., Liu, X., and Li, Y. (2023). Size Regulation of Polydopamine Nanoparticles by Boronic Acid and Lewis Base. Macromol. Rapid Commun. *44*, e2100916. https://doi.org/10.1002/marc.202100916.

18. Jin, A., Wang, Y., Lin, K., and Jiang, L. (2020). Nanoparticles modified by polydopamine: Working as "drug" carriers. Bioact. Mater. *5*, 522–541. https://doi.org/10.1016/j.bioactmat.2020.04.003.

19. Charmi, J., Nosrati, H., Mostafavi Amjad, J., Mohammadkhani, R., and Danafar, H. (2019). Polyethylene glycol (PEG) decorated graphene oxide nanosheets for controlled release curcumin delivery. Heliyon *5*, e01466. https://doi.org/10.1016/j.heliyon.2019.e01466.

20. Li, C., Chen, L., McClements, D.J., Peng, X., Qiu, C., Long, J., Ji, H., Zhao, J., Zhou, X., and Jin, Z. (2022). Preparation and Characterization of Rutin-Loaded Zein-Carboxymethyl Starch Nanoparticles. Foods *11*, 2827. https://doi.org/10.3390/foods11182827.

21. Rumpf, J., Burger, R., and Schulze, M. (2023). Statistical evaluation of DPPH, ABTS, FRAP, and Folin-Ciocalteu assays to assess the antioxidant capacity of lignins. Int. J. Biol. Macromol. *233*, 123470. https://doi.org/10.1016/j.ijbiomac.2023.123470.

22. Jain, K.K. (2020). An Overview of Drug Delivery Systems. Methods Mol. Biol. *2059*, 1–54. https://doi.org/10.1007/978-1-4939-9798-5_1.

23. Zhao, X., Sun, J., Dong, J., Guo, C., Cai, W., Han, J., Shen, H., Lv, S., and Zhang, R. (2022). An auto-photoacoustic melanin-based drug delivery nano-platform for self-monitoring of acute kidney injury therapy via a triple-collaborative strategy. Acta Biomater. *147*, 327–341. https://doi.org/10.1016/j.actbio.2022.05.034.

24. Mavridi-Printezi, A., Guernelli, M., Menichetti, A., and Montalti, M. (2020). Bio-Applications of Multifunctional Melanin Nanoparticles: From Nanomedicine to Nanocosmetics. Nanomaterials *10*. https://doi.org/10.3390/nano10112276.

25. Sun, T., Jiang, D., Rosenkrans, Z.T., Ehlerding, E.B., Ni, D., Qi, C., Kutyreff, C.J., Barnhart, T.E., Engle, J.W., Huang, P., and Cai, W. (2019). A Melanin-Based Natural Antioxidant Defense Nanosystem for Theranostic Application in Acute Kidney Injury. Adv. Funct. Mater. *29*. https://doi.org/10.1002/adfm.201904833.

26. Lin, L., Wang, S., Deng, H., Yang, W., Rao, L., Tian, R., Liu, Y., Yu, G., Zhou, Z., Song, J., et al. (2020). Endogenous Labile Iron Pool-Mediated Free Radical Generation for Cancer Chemodynamic Therapy. J. Am. Chem. Soc. *142*, 15320–15330. https://doi.org/10.1021/jacs.0c05604.

27. Kwon, K., Jung, J., Sahu, A., and Tae, G. (2022). Nanoreactor for cascade reaction between SOD and CAT and its tissue regeneration effect. J. Control Release *344*, 160–172. https://doi.org/10.1016/j.jconrel.2022.02.033.

28. Negahdari, R., Bohlouli, S., Sharifi, S., Maleki Dizaj, S., Rahbar Saadat, Y., Khezri, K., Jafari, S., Ahmadian, E., Gorbani Jahandizi, N., and Raeesi, S. (2021). Therapeutic benefits of rutin and its nanoformulations. Phytother. Res. *35*, 1719–1738. https://doi.org/10.1002/ptr.6904.

29. Liu, C., Zou, Q., Tang, H., Liu, J., Zhang, S., Fan, C., Zhang, J., Liu, R., Liu, Y., Liu, R., et al. (2023). Melanin nanoparticles alleviate sepsis-induced myocardial injury by suppressing ferroptosis and inflammation. Bioact. Mater. *24*, 313–321. https://doi.org/10.1016/j.bioactmat.2022.12.026.

30. Yan, H.-F., Tuo, Q.-Z., Yin, Q.-Z., and Lei, P. (2020). The pathological role of ferroptosis in ischemia/reperfusion-related injury. Zool. Res. *41*, 220–230. https://doi.org/10.24272/j.issn.2095-8137.2020.042.

31. Cui, Y., Pan, M., Ma, J., Song, X., Cao, W., and Zhang, P. (2021). Recent progress in the use of mitochondrial membrane permeability transition pore in mitochondrial dysfunction-related disease therapies. Mol. Cell. Biochem. *476*, 493–506. https://doi.org/10.1007/s11010-020-03926-0.

32. Bauer, T.M., and Murphy, E. (2020). Role of Mitochondrial Calcium and the Permeability Transition Pore in Regulating Cell Death. Circ. Res. *126*, 280–293. https://doi.org/10.1161/CIRCRESAHA.119.316306.

33. Bonora, M., Giorgi, C., and Pinton, P. (2022). Molecular mechanisms and consequences of mitochondrial permeability transition. Nat. Rev. Mol. Cell Biol. *23*, 266–285. https://doi.org/10.1038/s41580-021-00433-y.

34. Zhang, H., Yan, Q., Wang, X., Chen, X., Chen, Y., Du, J., and Chen, L. (2021). The Role of Mitochondria in Liver Ischemia-Reperfusion Injury: From Aspects of Mitochondrial Oxidative Stress, Mitochondrial Fission, Mitochondrial Membrane Permeable Transport Pore Formation, Mitophagy, and Mitochondria-Related Protective Measures. Oxid. Med. Cell. Longev. *2021*, 6670579. https://doi.org/10.1155/2021/6670579.

35. Liu, H., Yang, Y., Liu, Y., Pan, J., Wang, J., Man, F., Zhang, W., and Liu, G. (2020). Melanin-Like Nanomaterials for Advanced Biomedical Applications: A Versatile Platform with Extraordinary Promise. Adv. Sci. *7*, 1903129. https://doi.org/10.1002/advs.201903129.

36. Wu, Z., Yuan, K., Zhang, Q., Guo, J.J., Yang, H., and Zhou, F. (2022). Antioxidant PDA-PEG nanoparticles alleviate early osteoarthritis by inhibiting osteoclastogenesis and angiogenesis in subchondral bone. J. Nanobiotechnol. *20*, 479. https://doi.org/10.1186/s12951-022-01697-y.

37. Ozlu, B., Kabay, G., Bocek, I., Yilmaz, M., Piskin, A.K., Shim, B.S., and Mutlu, M. (2019). Controlled release of doxorubicin from polyethylene glycol functionalized melanin nanoparticles for breast cancer therapy: Part I. Production and drug release performance of the melanin nanoparticles. Int. J. Pharm. *570*, 118613. https://doi.org/10.1016/j.ijpharm.2019.118613.

STAR★METHODS

KEY RESOURCES TABLE

REAGENT or RESOURCE	SOURCE	IDENTIFIER
Chemicals, peptides, and recombinant proteins		
Dopamine hydrochloride, 98%	Aladdin, China	CAS#51-61-6
Rutin hydrate	Macklin, China	CAS#153-18-4
Lipopolysaccharides	Solarbio, China	CAS#L8880
NH2-mPEG-NH2, MW 1000, 98%	Macklin, China	CAS#N902461-1g
Fetal bovine serum	Thermo Fisher Scientific, USA	CAS#A5669701
Dulbecco's modified Eagle medium	Thermo Fisher Scientific, USA	CAS#11965092
penicillin-streptomycin solution	Thermo Fisher Scientific, USA	CAS#15140122
trypsin-EDTA	Thermo Fisher Scientific, USA	CAS#12605036
Phosphate-buffered saline	Thermo Fisher Scientific, USA	CAS#C10010500BT
4',6-diamidino-2-phenylindole	Beyotime, China	CAS#28718-90-3
lactic acid dehydrogenase	Beyotime, China	CAS#C0016
The BODIPY 581/591 C11 probes	MCE, China	CAS#217075-36-0
Critical commercial assays		
The ABTS Free Radical Scavenging Capacity Assay Kit	Solarbio, China	CAS#BC4775
2,2-Diphenyl-1-picrylhydrazyl	Macklin, China	CAS#T930756
Cell Counting Kit-8	DOJINDO, China	CAS#CK04
Experimental models: Cell lines		
HK-2	ACTT	CAS#CRL-2190
Experimental models: Organisms/strains		
Mouse:C57BL/6JNifdc-begi	Zhuhai BesTest Bio-Tech Co,.Ltd.	RRID:CSTR:15497.09.N000007
Mouse:BALB/cCrSlcNifdc	Zhuhai BesTest Bio-Tech Co,.Ltd.	RRID:CSTR:15497.09.N000009
Software and algorithms		
ImageJ	N/A	https://imagej.nih.gov/ij/
Prism	GraphPad	https://www.graphpad.com

RESOURCE AVAILABILITY

Lead contact

Inquiries and requests for resources should be directed to and will be fulfilled by the lead contact, Dr.Ding Liu, E-mail: banbybear01@smu.edu.cn.

Materials availability

Materials generated in this study can be made available upon reasonable request to the lead contact.

Data and code availability

Data

Data reported in this paper will be shared by the lead contact upon request.

Code

This paper does not report original code.

Data availability statement

Any additional information required to reanalyze the data reported in this paper is available from the lead contact upon request.

EXPERIMENTAL MODEL AND STUDY PARTICIPANT DETAILS

Mouse treatment

The male C57BL6/J mice (Zhuhai BesTest Bio-Tech Co,.Ltd.) were used in this study. Mice were aged 8 weeks. Gender had no significant effect on the experiment. All mice were group housed with a 12 hour–12 hour light-dark cycle, in which lights were turned on at 07:00 and turned off at 19:00. Food and water were available *ad libitum* and mice weighed between 20 and 25g.

Animal model construction

C57BL6/J mice (male) were divided into four groups, including a sham group, model (positive group, PP group, and PPR group). The positive group underwent right kidney resection and left kidney IRI. The mice were weighed and anesthetized via intraperitoneal injection. After anesthesia, the back area on both sides was prepared and disinfected with alcohol (from the lower border of the thoracic arch to the base of the tail). The mouse was placed in a prone position on a 37–38°C constant temperature heating pad. A left-sided incision was made along the spine to isolate and ligate the renal hilum, followed by removal of the left kidney and disinfection. The left kidney was isolated and the renal artery and vein were exposed. The renal artery was clamped for 1 min using a noninjurious Vascular clamp. The kidney gradually changed color from bright red to purple-brown. The mice were then placed back in the abdominal cavity and observed for 30 min. The wound was then covered with gauze to maintain the body temperature at 37–38°C. After the surgery, 500 μL of 0.9% sodium chloride injection was injected into the abdominal cavity to prevent dehydration. The abdominal wall and muscles were sutured using 5-0 sutures. The sham group did not undergo left renal artery clamping, and all other procedures were identical to those used for the other groups.

Mice and ethics approval

The animal experiments and euthanasia were performed with the approval of the Institutional Animal Care and Use Committee of Southern Medical University (Certification No. K2020015). All procedures were performed in accordance with the Animal Welfare Law, Guidelines for the Care and Use of Laboratory Animals, and the regulations of the Office of Laboratory Animal Welfare.

Cell lines and primary cell cultures

The HK-2 cells was purchase from Haixing Biosciences. HK-2 cells were maintained in Dulbecco's Modified Eagle Medium (Gibco, USA) supplemented with 10% fetal bovine serum (Gibco) and 1% Penicillin–Streptomycin (Invitrogen) in a humidified incubator at 37°C and 5% CO_2. The cells were tested by Short Tandem Repeat (STR) to determine their genetic characteristics. The cells were tested negative for mycoplasma contamination.

METHOD DETAILS

Synthesis of PDA

The PDA nanoparticles were synthesized according to the previous study.[17,35] Briefly, 432 mg of dopamine hydrochloride (2.28 mmoL) was dissolved in deionized water (216 mL). Then, 2280 μL of NaOH was added, and the mixture was stirred rapidly at 50°C for 10 h to obtain PDA NPs. The mixture was then centrifuged at 14,000 rpm and 26°C for 10 min, followed by three washes with deionized water.

Surface modification of PDA with NH2-PEG-NH2

PDA NPs (25 mg) were dissolved in deionized water (5 mL).[36] Then, 100 mg of Double-ended aminopolyethylene glycol (NH_2-PEG-NH_2) was added and the mixture was stirred vigorously at room temperature for 8 h to obtain PEG-modified PDA NPs (also called PEG-PDA NPs or PP NPs).[37] The mixture was then centrifuged at 12,000 rpm and 26°C for 10 min, followed by three washes with deionized water to remove unbound PEG molecules.

Rutin loading

PP NPs (25 mg) were dissolved in deionized water (5 mL). Rutin (25 mg) was added, and the mixture was stirred at room temperature for 24 h to obtain rutin-loaded PEG-PDA NPs (PPR NPs). The mixture was then centrifuged at 12,000 rpm and 26°C for 10 min, followed by three washes with deionized water to remove unbound rutin. Finally, the PPR NPs were obtained. The rutin supernatant was collected, and the absorbance of unloaded rutin was measured using a Ultraviolet Visible spectrophotometer (UV-Vis spectrophotometer). Different concentrations of rutin solution were prepared and absorbance was measured at 359 nm. The loading efficiency of rutin onto the PP NPs (expressed as a percentage) was calculated as the amount of rutin loaded divided by the amount of added rutin multiplied by 100.

Drug loading of PEG-PDA@rutin

Rutin solutions with mass concentrations of 180, 200, 220, and 240 μg/mL were prepared using ddH_2O. The absorbance of the solutions was measured at a wavelength of 363 nm using a UV-Vis spectrophotometer, and a standard curve of rutin solution absorbance (y) versus mass concentration (x) was plotted (Y = 0.02577*X - 1.593, R^2=0.9799). 2 mL of the supernatant obtained from PPR was diluted to an appropriate

concentration, and the absorbance at 350 nm was measured. The content of rutin in the supernatant during the drug loading process was then calculated based on the standard curve. The drug loading capacity (LC) of the material was calculated according to Equation 1.

$$LC\% = (M_1 - M_2) / M*100 \qquad \text{(Equation 1)}$$

M1 is the dosage mass of rutin, M2 is the mass of rutin in the supernatant, M is the mass of PP NPs, and the unit is milligram (mg).

Drug release assay of PEG-PDA@rutin

We sealed 2 mL of PPR in a dialysis bag (with a molecular weight cut-off of 10,000), and then immersed it in beakers containing 100 mL of ddH$_2$O and 500 μM H$_2$O$_2$, respectively. Tubes were placed on a magnetic stirrer and stirred at 37°C and 200 rpm. At specific time-points (0, 1, 2, 4, 6, 8, 12, 24 h), we removed 2 mL of the supernatant, replenished with 2 mL of the corresponding solution, and measured the absorbance of the extracted supernatant using a UV-Vis spectrophotometer. Calculated the amount of rutin released at different time points based on the rutin standard curve equations (H$_2$O Release: Y = 0.00198X + 0.218, R^2=0.992, H$_2$O$_2$ Release: Y = 0.002251X + 0.04505, R^2=0.9922). All experiments were repeated three times.

Characterization of PDA-based nanoparticles

The morphology of the designed NPs was characterized using transmission electron microscopy (TEM) (JEOL JEM-2100F TEM, Tokyo, Japan). A Shimadzu UV-2600 UV-vis spectrophotometer (Kyoto, Japan) was used to acquire spectra. The hydrodynamic diameters and zeta potentials were measured using a Zetasizer Nano ZS (Malvern, Worcestershire, UK) via dynamic light scattering (DLS). Fourier-transform infrared (FTIR) spectra were acquired using an FTIR spectrometer (Thermo Nicolet iS5).

The free radical-scavenging capabilities of rutin, PP NPs, and PPR NPs were tested using DPPH and ABTS radical cation decolorization assays. DPPH and ABTS radical solutions were prepared according to the manufacturer's instructions (MEC company, Japan). Then, the rutin, PP, and PPR solutions were mixed with DPPH or ABTS radical solution (final concentrations of 5, 10, 20, 30, 40, 50, 70, 90, 100, 120, 140, 160, 200, 220 μg/mL) and incubated for 30 mins in the dark. After incubation, the supernatant was transferred to a 96-well plate and absorbance was detected using an enzyme-labeled instrument.

Cell culture

Human kidney epithelial cells (HK-2) were seeded at a density of 1×10^5 cells/cm^2 in confocal dishes and cultured in DMEM containing 10% FBS at 37°C. To construct an *in vitro* IRI model, HK-2 cells were treated with LPS (1 μg/mL) for 18 h, or paced in anoxic incubator for stimulation for 24h, and the medium was then replaced with equal volumes of different solutions.

Cellular uptake

Rho-labeled PPR NPs were added to LPS-treated HK-2 cells and co-incubated for 1–8 h. The cells were fixed with 4% formaldehyde for 15 min and washed three times with PBS. The nuclei were stained with DAPI and washed three times. PPR NP uptake by HK-2 cells was observed and images were captured using an Olympus FV3000 confocal laser scanning microscope (CLSM, Olympus, Tokyo, Japan).

Cell toxicity

HK-2 cells were divided into four groups (control, stimulated, PP, and PPR) for cultivation. The control group was cultured normally, whereas the other three groups were subjected to LPS stimulation or anoxic incubator. After cultivation, PP and PPR NPs were added at a concentration of 100 μg/mL for 24 h to evaluate their therapeutic effects on IRI by Cell-Counting-Kit-8 (CCK-8) and lactic acid dehydrogenase (LDH) assays. Cells were washed with PBS and incubated with medium containing 10% FBS for 2 h or 60 μL of LDH detection working solution. Finally, absorbance was measured using an enzyme-linked immunosorbent assay (ELISA) plate reader.

ROS removal experiment

To detect ROS, LPS-treated HK-2 cells were co-cultured with various concentrations of PPR NPs (100 μg/mL) for 24 h, co-incubated with DCFH-DA (Beyotime) and the ROS detection reagent, and observed under a fluorescence microscope.

Ferroptosis detection

LPS-stimulated HK-2 cells were treated with PP and PPR NPs. After incubation, BODIPY 581/591 C11 probes were added to all four groups and incubated for 30 min. After the completion of the reaction, the culture medium was removed and the cells were washed three times with PBS. Fluorescence was measured and photographed using a fluorescence microscope, followed by a quantitative analysis using Image J.

Mitochondrial status detection

LPS-stimulated HK-2 cells were treated with PP and PPR NPs. After incubation, the cells were harvested and analyzed using the JC-1 Kit (KeyGen), MitoROS Kit (AAT Bioquest, Wuhan, China), mPTP (Mitochondrial Permeability Transition Pore) Kit (BestBio, Shanghai, China), and MitoCheck Complex I Activity Assay Kit (I-V) (Aimei, Wuhan, China).

In vivo distribution of PPR NPs on IRI mice

To evaluate the *in vivo* distribution of PPR NPs, IRI mice were injected with IR820-labeled PPR NPs through the tail vein. Fluorescence images of the whole body and major organs were obtained using a fluorescence imaging system (Digital Fluorescence Medicine Company, Beijing, China) under near-infrared (NIR) light.

Mouse sample collection and renal function testing

The mice were observed, and their conditions were recorded after surgery. A blood sample of 600–700 μL was collected via retro-orbital sinus after anesthesia and placed in a 2 mL purple-capped EDTA-containing anticoagulant tube. After centrifugation at 3000 r/min for 10 min, the supernatant was sent to the laboratory department of Zhujiang Hospital of Southern Medical University to test for blood creatinine and urea nitrogen levels. The left kidney was removed from the lower pole of the renal capsule and placed in 10% paraformaldehyde for Masson staining.

Histological examination and renal tubular injury scoring

The kidneys were fixed with 10% paraformaldehyde, dehydrated, embedded in paraffin, and sectioned for hematoxylin-eosin staining (HE), immunohistochemistry (IHC) and Masson staining. Ten non-overlapping fields were randomly selected under a 200× microscope, including five from the renal cortex and five from the corticomedullary junction.

QUANTIFICATION AND STATISTICAL ANALYSIS

Statistical analyses were performed using GraphPad Prism 9, and illustrations were created using Adobe Illustrator and Photoshop. Data are presented as means $\pm$ standard deviations. Comparisons between groups were performed using an independent samples *t*-test or a one-way ANOVA. Statistical significance was set at $P < 0.05$.